



On the Reynolds-Averaged Navier-Stokes Modelling of the Flow around a Simplified Train in Crosswinds

T. Li[†], J. Zhang¹, M. Rashidi² and M. Yu³

¹ State Key Laboratory of Traction Power, Southwest Jiaotong University, Chengdu610031, China

² School of Engineering, University of Birmingham, Birmingham B15 2TT, U.K.

³ College of Mechanical and Electrical Engineering, Qingdao University, Qingdao266071, China

[†]Corresponding Author Email: litian2008@home.swjtu.edu.cn

(Received March 7, 2018; accepted September 5, 2018)

ABSTRACT

Currently, there are different computational fluid dynamic (CFD) techniques used to obtain the flow around trains. One of these techniques is the Reynolds-averaged Navier-Stokes (RANS), which is commonly and widely used by industry to obtain the mean flow field around trains in different operating conditions. In order to assess the performance of RANS turbulence modelling for train aerodynamics, five different common RANS modelling have been used in this paper to obtain the flow and the surface pressure around a simplified train model subjected to crosswind; the standard $k-\varepsilon$ model, the realisable $k-\varepsilon$ model, the Re-Normalisation Group (RNG) $k-\varepsilon$ model, the standard $k-\omega$ model and Shear Stress Transport (SST) $k-\omega$ model. The train model was stationary and subjected to crosswind with a 90° yaw angle. The effects of mesh size and spatial discretization scheme on the aerodynamic characteristics of the train were also investigated. The results obtained from the different RANS models were compared to those from published experimental data. In general, all the RANS models provided the pressure distribution trend. However, all $k-\varepsilon$ models overestimate the surface pressure on the train body except the bottom face. The standard $k-\omega$ model underestimates the surface pressure on the train body except the streamwise face. It was shown that the simulation using SST $k-\omega$ model together with a second order discretization scheme provides the closest results to the experimental surface pressure. It could be concluded from the present study that the SST $k-\omega$ model with a second order discretization scheme and y^+ around 1.0 is the most appropriate RANS model for simulating the flow around trains subjected to crosswinds.

Keywords: RANS; Crosswind; Aerodynamics; Train; Flow.

NOMENCLATURE

A_y	projected area of the simplified train in the y direction	n	constant coefficient
A_z	projected area of the simplified train in the z direction	p	static pressure
C_l	aerodynamic lift force coefficient	p_∞	reference pressure
C_p	pressure coefficient	\mathbf{u}	velocity at the inlet boundary
C_s	aerodynamic side force coefficient	u_{in}	lateral velocity at the inlet boundary
c	constant	u	incoming flow velocity
D	height of the simplified train body	ρ	air density
F_l	aerodynamic lift force	Re_L	Reynolds number
F_s	aerodynamic side force	μ	dynamic viscosity

1. INTRODUCTION

With the increase in train speed and the trend of decreasing weight of high-speed trains, the subject of stability of trains in crosswinds has received a considerable attention of many researchers in the

last three decades (Ding *et al.*, 2008; Baker, 2010; Li *et al.*, 2015). Indeed the crosswind assessment is now a main part of the train regulations in British Standard EN 14067-6 code (BS EN, 2010). There are generally three different methodologies for the investigation of train stability in crosswinds: full-

scale tests, physical modelling and numerical modelling using computational fluid dynamics.

According to the authors' knowledge, a few full-scale experiments have been carried out for crosswind assessment. Baker *et al.* (2004) measured the mean and peak aerodynamic forces and moments on a full-scale train and compared the results with wind tunnel experimental data. It was found that the agreement in rolling moment coefficients was good. In addition, crosswind assessment has been done on a full-scale train as part of the TRANSAERO (A European Initiative on Transient Aerodynamics for Railway System Optimisation) project (Matschke *et al.*, 2002). Xiong *et al.* (2006) and Liu *et al.* (2018) measured the train surface pressure using a vehicle-mounted pressure test system when high-speed trains running on the Lanzhou-Xinjiang railway were subjected to crosswinds. Although full-scale experiments represent reality, they are difficult to perform and researchers have no control of the atmospheric winds such as yaw angle, wind speed and turbulence intensity (Schetz, 2001).

Most of the physical modelling investigations have been carried out using the traditional wind tunnel measurements (Copley, 1987; Chiu *et al.*, 1992; Suzuki *et al.*, 2003; Cheli *et al.*, 2010) with some exceptions of using a moving train rig (Baker *et al.*, 2001; Dorigatti *et al.*, 2015). Conventional wind tunnel experiments were reported for measuring the aerodynamic forces of stationary train models (Suzuki *et al.*, 2003; Boccione *et al.*, 2008; Cheli *et al.*, 2010; Morden *et al.*, 2015). The stationary wind tunnel technique is the most widely used for train aerodynamic testing. In order to investigate the situation of the relative motion between the ground and train, the moving model rig facility is normally used (Cooper, 1981; Baker, 1986; Baker *et al.*, 2001; Dorigatti *et al.*, 2015) to obtain the aerodynamic coefficients. Although wind tunnel technique is widely used for crosswind assessment, it suffers from issues related to the scale effect and the limitations of measurements on points and lines. The technique is also limited in terms of visualizing the 3D vortices around trains and how these vortices affect the aerodynamic performance in crosswinds.

Due to the high cost of aerodynamic experiments and the development of high performance computational resources, CFD simulation has become more popular in train aerodynamics. It is now one of the approved methods for train crosswind assessment in the European Committee for Standardization (CEN) and TSI codes. Aerodynamic forces and moments acting on trains were presented by means of numerical simulations. The realisable $k-\epsilon$ model with wall functions was adopted to simulate aerodynamic forces acting on a high-speed train (Cheli *et al.*, 2010). Premoli *et al.* (2016) investigated the effect of the relative motion between train and infrastructure using SST $k-\omega$ model. Diedrichs *et al.* (2007) studied the crosswind stability for Inter-City Express (ICE) high-speed train running on an embankment using the standard $k-\epsilon$ and quadratic $k-\epsilon$ turbulence

models. Liu *et al.* (2018) used SST to investigate the aerodynamics of a high-speed train passing through a windbreak under crosswind. Diedrichs (2003) investigated the effect of different $k-\epsilon$ turbulence models and numerical schemes on the crosswind stability of trains. Both quadratic $k-\epsilon$ model and detached-eddy simulation (DES) were applied to resolve the flow around a train subjected to crosswinds (Diedrichs, 2010). Morden *et al.* (2015) studied the surface pressure on a Class 43 high-speed train by means of five different RANS models and DES. The SST $k-\omega$ and DES models were tested for their ability to predict the flow field around and aerodynamic forces on a train in crosswinds by Li *et al.* (2018). Maleki *et al.* (2017) assessed various turbulence modelling approaches to study the air flow around a freight train including SST $k-\omega$ model and DES. DES simulations of the slipstream of trains were carried out (Flynn *et al.*, 2014; Huang *et al.* 2014). The effect of the shape of the nose on the aerodynamic forces on and flow structures around a simplified train shape subjected to crosswind was studied using the large-eddy simulation (LES) (Hemida *et al.*, 2008; Hemida and Krajnovic, 2010). Hemida *et al.* (2005) studied the flow around the same train model of Copley (1987) under crosswind using LES and concluded that LES gives accurate results compared to the experimental data. Hemida and Baker (2010) and Östth and Krajnović (2010) studied the aerodynamics of a container freight wagon using the DES and LES. García *et al.* (2015) investigated the flow structures around a simplified ICE2 without inter-car gaps and bogies using LES.

Although the time resolving CFD techniques such as LES and DES gives large data set that can be used to understand the flow around trains in both time and space, they are computationally expensive and cannot be widely used for parametric studies in train aerodynamics. On the other hand, RANS simulations are cheap to perform and indeed they are the current approved CFD technique in both industry and the CEN and TSI codes for train assessment in crosswind. However, the results of RANS simulations depend on many different parameters including the RANS modeling, the discretization scheme and the mesh quality. In this paper, the effects of these parameters are investigated through a series of numerical experiments using five common RANS models with different discretization schemes and mesh quality. The main aim is to find the behaviour of each model on predicting the flow and surface pressure at different parts of and around the train model. The simplified train model of Copley (1987) has been candidate for the fundamental work in this paper and experimental data of Chiu *et al.* (1992) is used to validate the numerical results. The simulation has been carried out using the commercial software ANSYS Fluent.

The present paper is structured as follows. Section 2 describes the physical model of a simplified train. The RANS models are presented in Section 3. The numerical model including the computational

domain, computational mesh and numerical method is described in Section 4. The effect of mesh size, spatial discretization scheme and RANS model on the aerodynamic characteristics is discussed in Section 5. Section 6 reports the comparisons of aerodynamic characteristics between SST $k-\omega$ model and LES. And conclusions are drawn in Section 7.

2. PHYSICAL MODEL

The simplified train model used by Chiu *et al.* (1992) and Hemida *et al.* (2005, 2008) is chosen for this investigation. The model made up of a streamline nose and a train body had a slenderness ratio of 10, as shown in Fig. 1.

The train body is cylindrical, and its cross-sectional profile is defined by:

$$|y|^n + |z|^n = c^n, \quad (1)$$

where $c = 62.5$ mm and $n = 5$. The height of the train body D is 125 mm, and the total length of the train is $9.36D$.

The cross-section of the train nose becomes smaller and circular towards the nose tip (Fig. 1(a)) and its cross-sectional profile is also given by Eq. (1) with different parameters. The parameter n decreases uniformly to 2 at the nose tip, and the parameter c follows a semi-elliptical profile with a major diameter of $1.28D$.

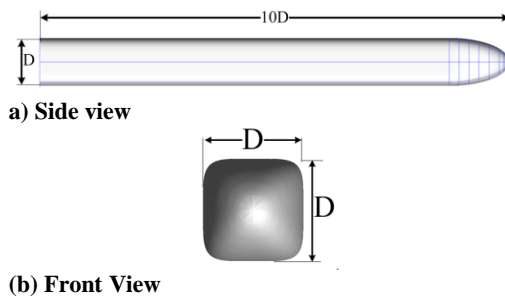


Fig. 1. The simplified train model.

3. REYNOLDS-AVERAGED NAVIER-STOKES

In general, the Mach number of the air flow around a typical high-speed train is less than 0.3, therefore, the flow can be assumed incompressible. In this case, the continuity equation as well as the incompressible Navier-Stokes equations represent the governing equations of the flow around trains. The temporal terms in Navier-Stokes equations are neglected as only the steady RANS simulations are investigated in this study. The most commonly used two-equation RANS models are the $k-\varepsilon$ and $k-\omega$, which will be explained briefly in the following sections.

The $k-\varepsilon$ model gives a general description of turbulence with two transported variables, which are the turbulent kinetic energy k and the turbulent

dissipation ε , respectively. Three typically $k-\varepsilon$ models studied in this paper are the standard $k-\varepsilon$ model, the realisable $k-\varepsilon$ model and the RNG $k-\varepsilon$ model.

The $k-\omega$ model is also a two equation model. The two transported variables are the turbulent kinetic energy k and the specific dissipation rate ω , respectively. Two typical $k-\omega$ models discussed in this paper are the standard $k-\omega$ model and the SST $k-\omega$ model, respectively.

4. NUMERICAL MODEL

4.1 Computational Domain

The computational domain shown in Fig. 2 has a streamwise length of $29D$, a spanwise width of $13.4D$ and a height of $9.76D$. The computational domain consists of an inlet, outlet and 4 side walls. Similar to the experiment, the train is mounted in the side wall of the domain. The vertical distance between the train and the ground is $0.15D$. The computational domain is consistent to the experimental set-up of Chiu *et al.*, (1992) and that of Hemida *et al.* (2005). It should be noted that the rear part of the train is close to the wind tunnel wall in the experiment test (Chiu *et al.*, 1992), therefore, the pressure on the front part of the train is the most concerned in this study. In addition, a mesh refinement region is established around the train to obtain flow physics in the boundary layer. The region has a length of $12D$ along the train, a width of $2D$ and a height of $1.65D$.

A uniform velocity, $\mathbf{u} = (0, 0, u_{in})$, is specified at the inlet boundary. A zero-pressure condition is prescribed at the outlet boundary, and the no-slip boundary condition is imposed at all walls and train surface.

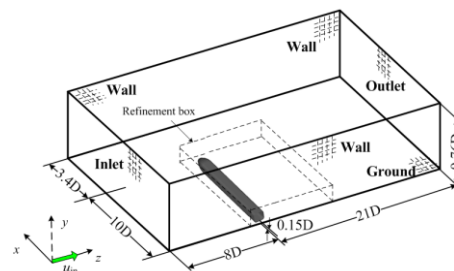


Fig. 2. Computational domain.

Several loops shown in Fig. 3(a) are defined along the train surface. The surface pressures at these loops are compared with the experimental ones for validation (Chiu *et al.*, 1992). The pressure distribution on a specific loop is displayed in a polar coordinate. The pole is defined as the centre of the cross-section as shown in Fig. 3(b).

4.2 Computational Mesh

A trimmed mesh (generated by cutting a hexahedral template mesh with the geometry surface), which is mainly combined by the hexahedral cells is generated.

Table 1 Different trimmer meshes used in the investigation

	Cell size of the train surface (mm)	First cell height off the train (mm)	Number of prism layers	Number of cells (million)	y+
mesh1	2.0	0.8	12	6.45	40.0
mesh2	1.0	0.8	12	16.90	40.0
mesh3	1.0	0.08	18	19.12	4.0
mesh4	1.0	0.05	22	26.14	2.5

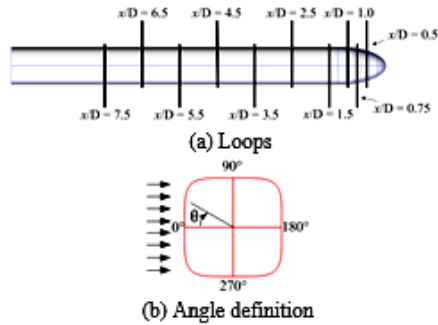


Fig. 3 Loops and angle definition

Figure 4 shows the mesh around the train at a cross-section $x/d = 6.5$. The mesh is refined in a refinement region around the model. Different boundary layer meshes are created around the train surface. Four different hexahedral meshes were generated with different parameters (Table1). The cell size of the train surface in both spanwise and streamwise directions is smaller than 2 mm.

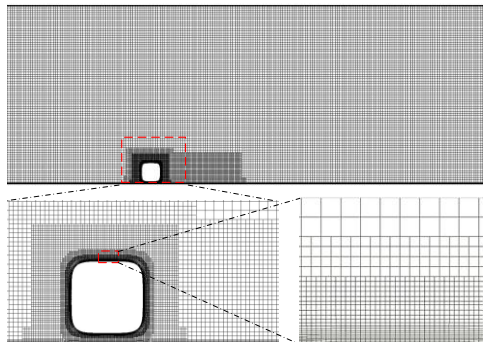


Fig. 4. Trimmed mesh around the train.

4.3 Numerical Method

The commercial software FLUENT was used to obtain the flow and the surface pressure around a simplified train model subjected to crosswinds. The Finite Volume Method (FVM) was adopted for the discretization of the governing equations. The Semi-Implicit Method for Pressure-Linked Equations (SIMPLE) algorithm was used to obtain the pressure and velocity fields. Different RANS models and spatial discretization schemes were chosen and compared in this study. Five different RANS models are the standard $k-\epsilon$ model, realisable $k-\epsilon$ model, RNG $k-\epsilon$ model, standard $k-\omega$ model and SST $k-\omega$ model. Different spatial discretization schemes for solving the momentum equations are the First Order Upwind, Second Order Upwind and Third-Order Monotonic Upstream-Centered Scheme for Conservation Laws (MUSCL).

The standard wall function or enhanced wall treatment was chosen for all standard $k-\epsilon$ models. When y^+ is larger than 30.0, the standard wall function is advised; when y^+ is ~ 1.0 , the enhanced wall treatment is advised (FLUENT User's Guide, 2011).

5 RESULTS

The calculation parameters used in this study are similar to those used in the experiment of Chiu *et al.* (1992) and the previous numerical simulations of Hemida *et al.* (2005). These are listed in Table 2. The yaw angle between the crosswind and the simplified train is 90° . The Reynolds number is 300,000 based on the height of the simplified train D and the air flow velocity at the inlet boundary u_{in} .

Table 2 Calculation parameters

ρ (kg/m ³)	μ (N·s/m ²)	u_{in} (m/s)	Re _L
1.138	1.8584×10^{-5}	39.2088	300,000

5.1 Aerodynamic Coefficients

The aerodynamic side force coefficient C_s and lift force coefficient C_l are defined as:

$$C_s = \frac{F_s}{0.5 \rho u_\infty^2 A_z}, \quad (2)$$

and

$$C_l = \frac{F_l}{0.5 \rho u_\infty^2 A_y}, \quad (3)$$

where F_s and F_l are the aerodynamic side and lift forces, respectively; ρ is the air density; u_∞ is the incoming flow velocity, A_z and A_y are the projected areas of the simplified train in the vertical and lateral directions, respectively. $A_y = A_z = 0.1541 \text{ m}^2$.

The pressure coefficient C_p is defined as:

$$C_p = \frac{p - p_\infty}{0.5 \rho u_\infty^2}, \quad (4)$$

where p is the static pressure, p_∞ is the reference pressure, which is usually chosen at the inlet boundary.

5.2 Mesh Sensitivity

Mesh sensitivity is investigated by performing 4 numerical simulations with a different number of

cells. The mesh information is given in Table 1. The SST $k-\omega$ model is chosen for the simulation. Table 3 shows the force coefficients of the train obtained from the simulation using different meshes. In the near wall region, the y^+ of mesh1 and mesh2 is about 30.0, and the y^+ of mesh3 and mesh4 is ~ 1.0 . It indicates that the force coefficients are sensitive to the y^+ , especially for the lift force coefficient. The agreement between the force coefficients obtained from the mesh3 and mesh4 with a y^+ around 1.0 is generally good.

Table 3 Force coefficients obtained from the simulation using different meshes

Force coefficient	mesh1	mesh2	mesh3	mesh4
C_s	0.6195	0.6212	0.5187	0.5244
C_l	0.3597	0.1872	0.6117	0.6056

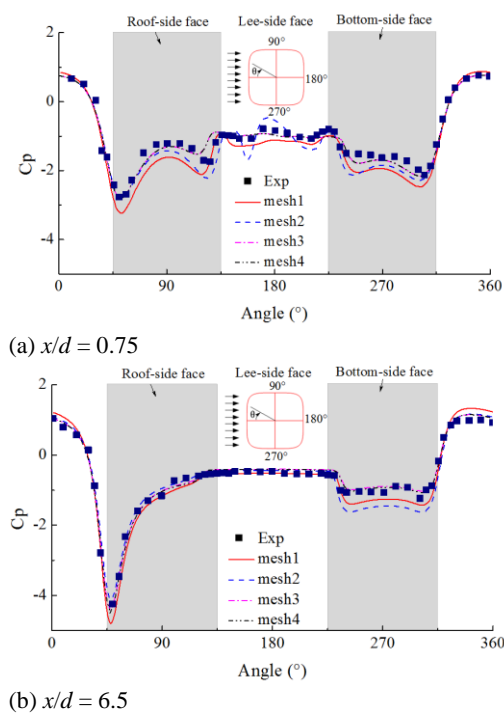


Fig. 5. Surface pressure distribution obtained from different meshes.

Figure 5 shows the surface pressure distribution obtained from different meshes at loops $x/d = 0.75$ and $x/d = 6.5$. It can be seen that the surface pressures along the loops obtained from the mesh3 and mesh4 show good agreement with the experimental results. All simulations give similar trends in the surface pressure distribution, however, a lower pressure obtained from mesh1 and mesh2 is observed on both bottom-side and roof-side faces. This pressure difference makes the lift force coefficient obtained from mesh1 and mesh2 lower than those obtained from mesh3 and mesh4. On the other hand, it is observed that a slightly larger pressure on the windward-side face and a slight lower averaged pressure on the lee-side face are obtained from mesh1 and mesh2. This pressure difference makes the side force coefficient C_l obtained from mesh1 and mesh2 larger than those obtained from mesh3 and mesh4.

The streamlines around the train projected onto the plane $x/d = 0.75$ colored by the velocity magnitude are shown in Fig. 6. All simulations give almost the same streamline trend around the train body. However, some minor differences in the magnitude of the velocity occur in the below of the bottom-side face and the above of the roof-side face. It is shown that the magnitude of velocity below the bottom-side face and above the roof-side face obtained from mesh1 and mesh2 is larger than that obtained from mesh3. This difference in the velocity makes the pressure on the bottom-side face and roof-side face lower than that obtained from mesh3. Meanwhile, the difference in velocity below the bottom-side face makes the boundary layer thickness obtained from mesh2 smaller than that obtained from mesh3. The pressure distribution and streamlines around the train on the plane $x/d = 6.5$ are also conducted and showed similarities to those on the plane $x/d = 0.75$. The agreement between mesh3 and mesh4 indicates that no further mesh refinement is needed and thus mesh3 is chosen to be used for the different simulations in this work.

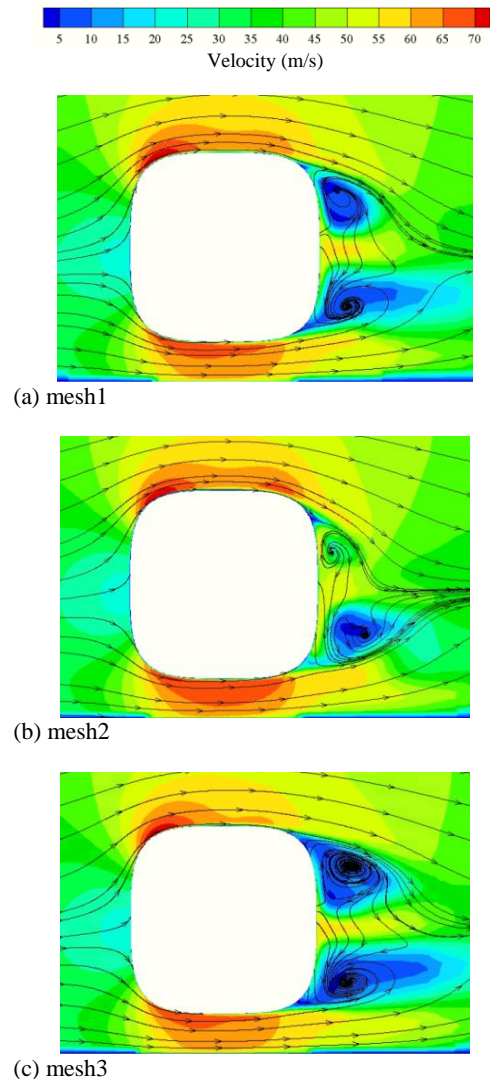


Fig. 6. Streamlines around the train projected onto the plane $x/d = 0.75$ colored by the velocity magnitude.

5.3 Spatial Discretization Scheme

It is very important to choose the proper spatial discretization scheme in CFD. In this section, the effect of spatial discretization scheme on aerodynamic results is analysed using the SST $k-\omega$ model. Several different schemes for different

variables are listed in Table 4, which are the first order (FO), second order (SO), high order (HO) and mixed order (MO) discretization schemes, respectively.

The force coefficients of the train calculated using

Table 4 Spatial discretization for different variables

Variable	First Order Discretization	Second Order Discretization	High Order Discretization	Mixed Order Discretization
Pressure	Linear	Second Order	Second Order	Linear
Momentum	First Order Upwind	Second Order Upwind	Third-Order MUSCL	Second Order Upwind
Turbulent kinetic energy	First Order Upwind	Second Order Upwind	Third-Order MUSCL	First Order Upwind
Turbulent dissipation rate	First Order Upwind	Second Order Upwind	Third-Order MUSCL	First Order Upwind

Table 5 Force coefficients for different spatial discretization schemes

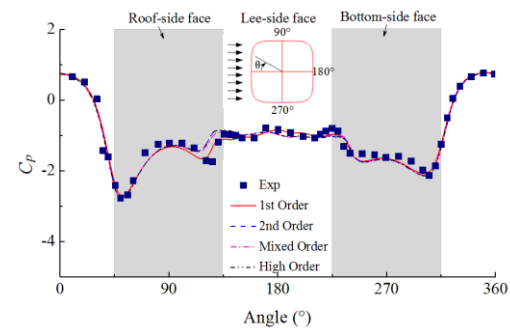
	FO		SO	HO		MO	
	Value	Error	Value	Value	Error	Value	Error
C_s	0.5847	12.72%	0.5187	0.5144	0.83%	0.5224	0.71%
C_l	0.5405	11.64%	0.6117	0.6180	1.03%	0.6191	0.18%

different spatial discretization schemes are given in Table 5. The percentage difference is obtained by the relative error between the 2nd order and other schemes. It can be seen that there is a considerable difference in aerodynamic coefficients obtained from the first order discretization scheme and the other schemes. The maximum differences in the force coefficients among the non-first order discretization schemes are less than 1.03%. Compared with the first order scheme and mixed order scheme, the spatial discretization scheme for momentum variables has a great effect on the aerodynamic coefficients.

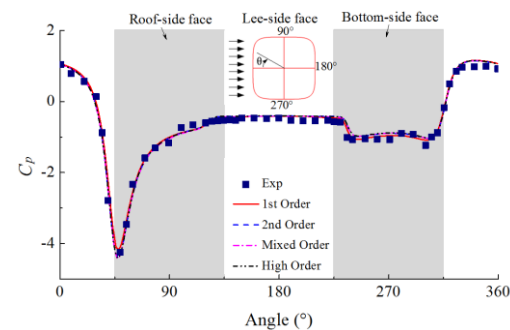
Figure 7 shows the effect of spatial discretization scheme on the surface pressure distribution. Two planes are $x/d = 0.75$ and $x/d = 6.5$. All simulations give almost the same pressure distribution trends. However, the pressure coefficient around an angle of 130° on the roof-side face obtained using the first order discretization is less than those obtained using the other schemes on the plane $x/d = 0.75$. By comparison with the pressure distribution obtained using the non-first order schemes, the minimum pressure coefficient obtained using the first order discretization is larger, and the pressure coefficient on the bottom-side face is less at the plane $x/d = 0.75$. At the same time, the minimum pressure coefficient occurred at the crossing of the roof-side face and the windward-side face affects both aerodynamic side and lift force coefficients. These differences in the pressure coefficient make the side force coefficient obtained using the first order discretization is larger than those obtained using the other schemes and the lift force coefficient smaller.

Compared to the experimental results, the second order, high-order and mixed discretization schemes

provide better accuracy than the first order in predicting the minimum pressure coefficient at the plane $x/d = 6.5$. This is due to the fact that the first order scheme is numerically dissipative and thus predicts less accurate results.



(a) $x/d = 0.75$



(b) $x/d = 6.5$

Fig. 7. Effect of spatial discretization schemes on surface pressure distribution.

In general, high-order discretization schemes provide slightly better accuracy than the first order

scheme. However, no significant differences have been found between second order and higher order discretization schemes used in RANS simulations. It should be noted that the third order MUSCL scheme could improve the spatial accuracy by reducing the numerical diffusion with comparison to the second-order schemes, however, its convergence and stability could be worse when the complex train geometry is applied.

5.4 Turbulence Modelling

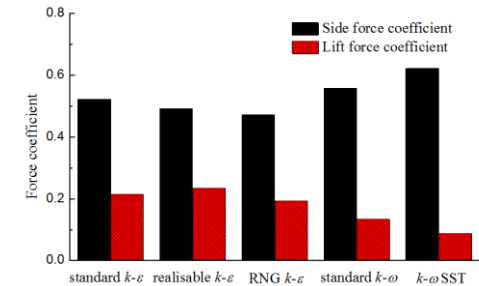
The transport equations for different RANS turbulence models are introduced in Section 3. It is a key factor to choose a proper turbulence model for accurate simulations. The effect of the turbulence model on aerodynamic results is discussed in this section using the second order discretization scheme. The effect of turbulence modelling has been investigated through the use of five different common RANS models; the standard $k-\epsilon$ model, the realisable $k-\epsilon$ model, the RNG $k-\epsilon$ model, the standard $k-\omega$ model and SST $k-\omega$ model. To reveal the effect of y^+ on the surface pressure distribution together with turbulence modelling, the aerodynamic characteristics obtained from mesh2 and mesh3 are also used in this Section.

The side force coefficient and lift force coefficient obtained using different turbulence models and meshes are shown in Fig. 8. It can be seen that there are major differences among the lift force coefficients obtained from different meshes. For all turbulence models when y^+ is around 30.0 and the standard wall function is adopted, the lift force coefficient is much smaller than the expected value 0.6117 (for simplicity the expected value is defined as the value obtained from the SST $k-\omega$ model with second order discretisation scheme and mesh3). However, when the standard $k-\epsilon$ model together with the standard wall function is adopted, the side force coefficient is close to the expected one. Although the lift and side coefficients obtained using all $k-\epsilon$ models together with the enhanced wall treatment are improved compared to results from the standard wall function, they still deviate from the expected one. Moreover, the standard $k-\omega$ model performs the second best among all turbulence modelling with a y^+ of around 1.0 compared to the expected value.

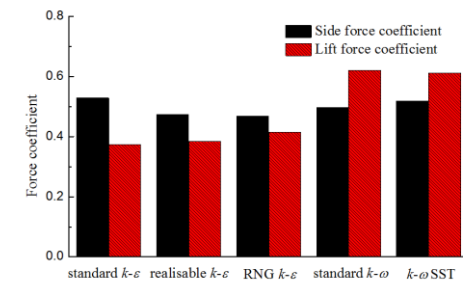
In order to explain the differences in force coefficients, the results are analysed in terms of surface pressure comparison with the experimental one and the flow field obtained from the different turbulence models are compared in the following section.

Firstly, the surface pressure distribution at different loops obtained using different RANS turbulence modelling together with mesh2 is shown in Fig. 9. It can be seen that all approaches have similar trends, which are similar to the experiment on both loops. However, all approaches failed to accurately replicate the experimental data on both roof-side and bottom-side faces. This deviation leads to the lift force coefficient obtained from mesh2 lower than the expected one. Moreover, there are larger

variations in the pressure distribution on the lee-side face at the loop $x/d = 0.75$ obtained using the standard $k-\epsilon$ model, RNG $k-\epsilon$ model and SST $k-\omega$ model than that of the experimental one. It has to be clarified here that the agreement in the side force coefficient is not due to the accurate prediction of the surface pressure but due to the compensation of the underestimation of the pressure on some regions and the overestimation of the pressure on other certain regions.

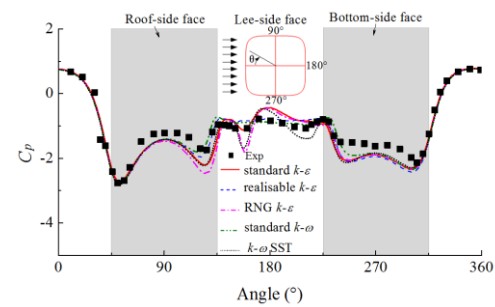


(a) mesh2

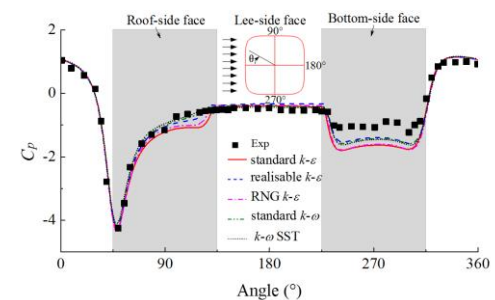


(b) mesh3

Fig. 8. Effect of turbulence modeling on the force coefficients.



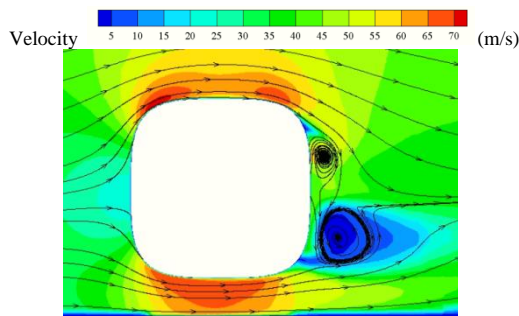
a) $x/d = 0.75$



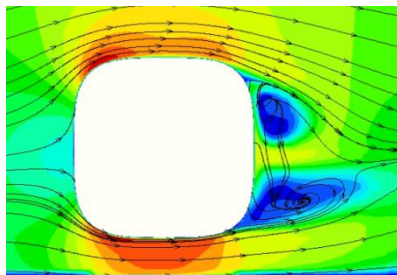
(b) $x/d = 6.5$

Fig. 9. Effect of turbulence modeling on the pressure coefficient distribution (mesh2).

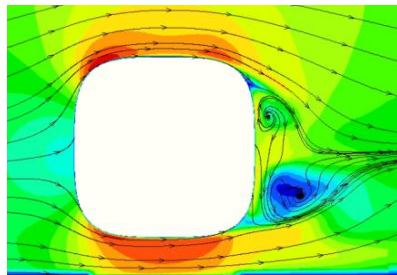
Figure 10 shows the streamlines around the train projected onto the plane $x/d = 0.75$ colored by the velocity magnitude. The results obtained from the realisable $k-\varepsilon$ model, RNG $k-\varepsilon$ model and SST $k-\omega$ model are shown in Fig. 10. Above the roof side face and under the train the realisable $k-\varepsilon$ model and SST $k-\omega$ model give similar flow field. However, a slightly different flow field has been noticed above the roof obtained from the RNG $k-\varepsilon$ model. The realisable $k-\varepsilon$ model and SST $k-\omega$ model give similar flow field with different velocity magnitude in the recirculation region behind the train model.



(a) realisable $k-\varepsilon$



(b) RNG $k-\varepsilon$

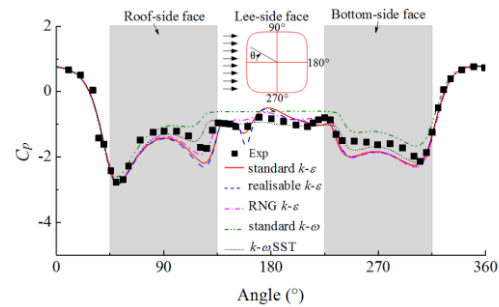


(c) SST $k-\omega$

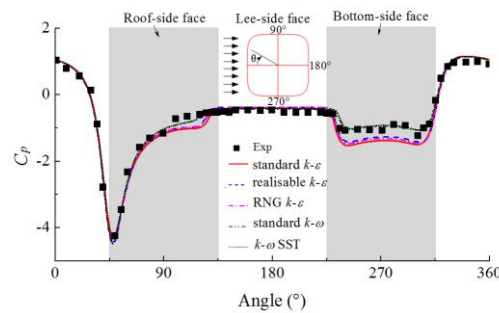
Fig. 10. Streamlines around the train projected onto the plane $x/d = 0.75$ colored by the velocity magnitude (mesh2).

Figure 11 shows the surface pressure coefficient distribution at different loops obtained using different RANS turbulence modelling on mesh3. On both roof-side and bottom-side faces, there are considerable differences in the predicted surface pressure by the RANS modelling, where the pressure obtained using the $k-\varepsilon$ models deviates from the experimental one. Therefore, the lift force coefficients obtained using the $k-\varepsilon$ models are different from the expected value. Moreover, the standard $k-\omega$ model underestimates the surface pressure on the train body except the windward face at the loop $x/d = 0.75$. Although the force

coefficients obtained using the standard $k-\omega$ model are close to the expected ones, it has to be clarified here that this agreement is not due to the accurate prediction of the surface pressure but due to the compensation of the underestimation of the pressure on some regions and the overestimation of the pressure on other certain regions. Among all the models, the SST $k-\omega$ model has the smallest difference between the experimental and the numerical pressure on both loops.



(a) $x/d = 0.75$



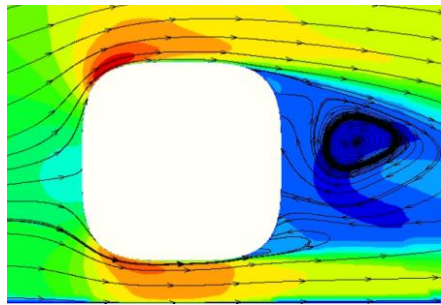
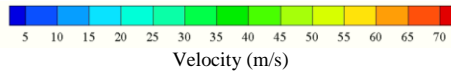
(b) $x/d = 6.5$

Fig. 11. Effect of turbulence modeling on the pressure coefficient distribution (mesh3).

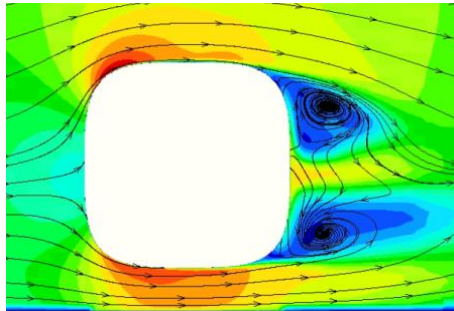
Figure 12 shows the streamlines projected onto the plane $x/d = 0.75$ colored by the velocity magnitude obtained using mesh3. There is a considerable difference in the flow field obtained using the standard $k-\omega$ model and SST $k-\omega$ especially in the wake flow. The standard $k-\omega$ model predicts a dominating upper vortex, and the SST $k-\omega$ model gives two similar vortices. These two similar vortices in the wake of the train generate variations in the surface pressure that has been noticed in Fig. 11(a). In addition to the variation in the wake flow, some minor differences in the velocity magnitude have been noticed in the flow above the roof-side face and under the train.

Figure 13 shows the streamlines around the train projected onto the plane $x/d = 6.5$ colored by the velocity magnitude obtained from mesh3. Both the standard $k-\varepsilon$ model and SST $k-\omega$ model give flow feature with two circulation regions. However, the sizes of the recirculation regions are different and the cores of the recirculation regions are far from the train surface in case of the SST $k-\omega$ turbulence modelling compared to that obtained using the standard $k-\varepsilon$ model. It explains the differences in the surface pressure around angles of 130° and 250° shown in Fig. 11(b).

By comparing the pressure predicted for mesh2 and mesh3, it is noted that all $k-\varepsilon$ models predict similar trends. However, the pressure obtained from mesh3 is more accurate than that obtained using mesh2. Compared with the results from mesh2 with a y^+ around 30.0, the pressure predicted from mesh3 with a y^+ around 1.0 is closer to the experimental one.

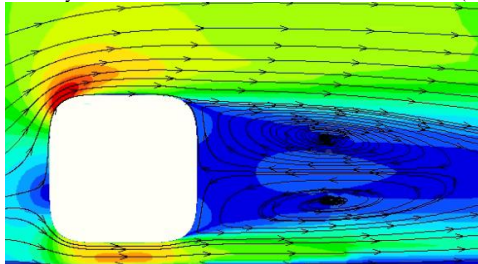
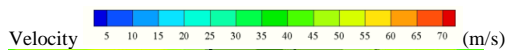


(a) standard $k-\omega$

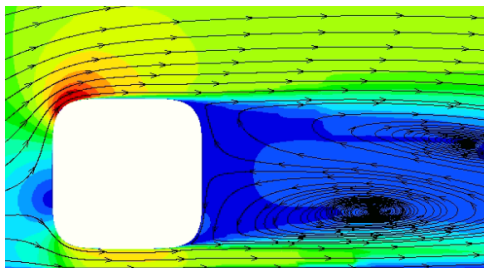


(b) SST $k-\omega$

Fig. 12. Streamlines around the train projected onto the plane $x/d = 0.75$ colored by the velocity magnitude (mesh3).



(a) standard $k-\varepsilon$



(b) SST $k-\omega$

Fig. 13. Streamlines around the train projected onto the plane $x/d = 6.5$ colored by the velocity magnitude (mesh3).

From what has been discussed above, we can draw the conclusion that the $k-\varepsilon$ turbulence models can not predict the pressure accurately on both the roof-side face and bottom-side face, therefore, the lift force coefficient deviates from the accurate one. The $k-\varepsilon$ turbulence models with both the standard wall function and the enhanced wall treatment can provide a reasonable side force coefficient. However, the pressure predicted on the lee-side face shows a certain deviation from the experimental data. Compared to the experimental results, among all turbulence modelling, the SST $k-\omega$ model with y^+ around 1.0 can provide accurate pressure distribution and aerodynamic forces of the trains subjected to crosswinds.

6. COMPARISONS OF AERODYNAMIC CHARACTERISTICS BETWEEN SST AND LES

Hemida *et al.* (2005) studied the flow around the simplified train model under crosswind using LES. In this section, the flow and the surface pressure using SST together with a low y^+ are compared with the previous ones using LES conducted by Hemida *et al.* (2005).

6.1 Pressure Distribution

Comparison of the pressure coefficient obtained from SST with the LES data of Hemida *et al.* (2005) and experimental results (Chiu *et al.*, 1992) at different loops is shown in Fig. 14. Compared to the experimental results, there are slight differences in pressure on the roof-side, lee-side and bottom-side faces of the train nose. When $x/d \geq 3.5$, the pressure profiles are almost constant and no changes have been noticed at any planes. This is consistent with the LES results reported by Hemida *et al.* (2005) and the experimental results (Chiu *et al.*, 1992). Both SST and LES are able to reproduce accurate pressure results on almost all loops when compared to experimental data. Compared to the LES results, the SST $k-\omega$ model predicts more accurate pressure on the bottom-side face at all loops except the $x/d = 0.5$.

6.2 Time Averaged Flow Characteristics

The flow separates and reattaches around the train at a high Reynolds number. Figure 15 shows the cores of the recirculation and separation regions around the train. The cores of these regions in the wake flow can be described as follows:

- (1) The cores of the vortices V_1 and V_3 almost stretch along the whole train.
- (2) The core of the vortex V_2 originates from the nose of the train.
- (3) The cores of the vortices V_4 and V_5 are far from the lee side surface of the train, which are generated by the extrusion and split between two attached vortices.
- (4) The core of the vortex V_6 appears near the side wall of the wind tunnel.

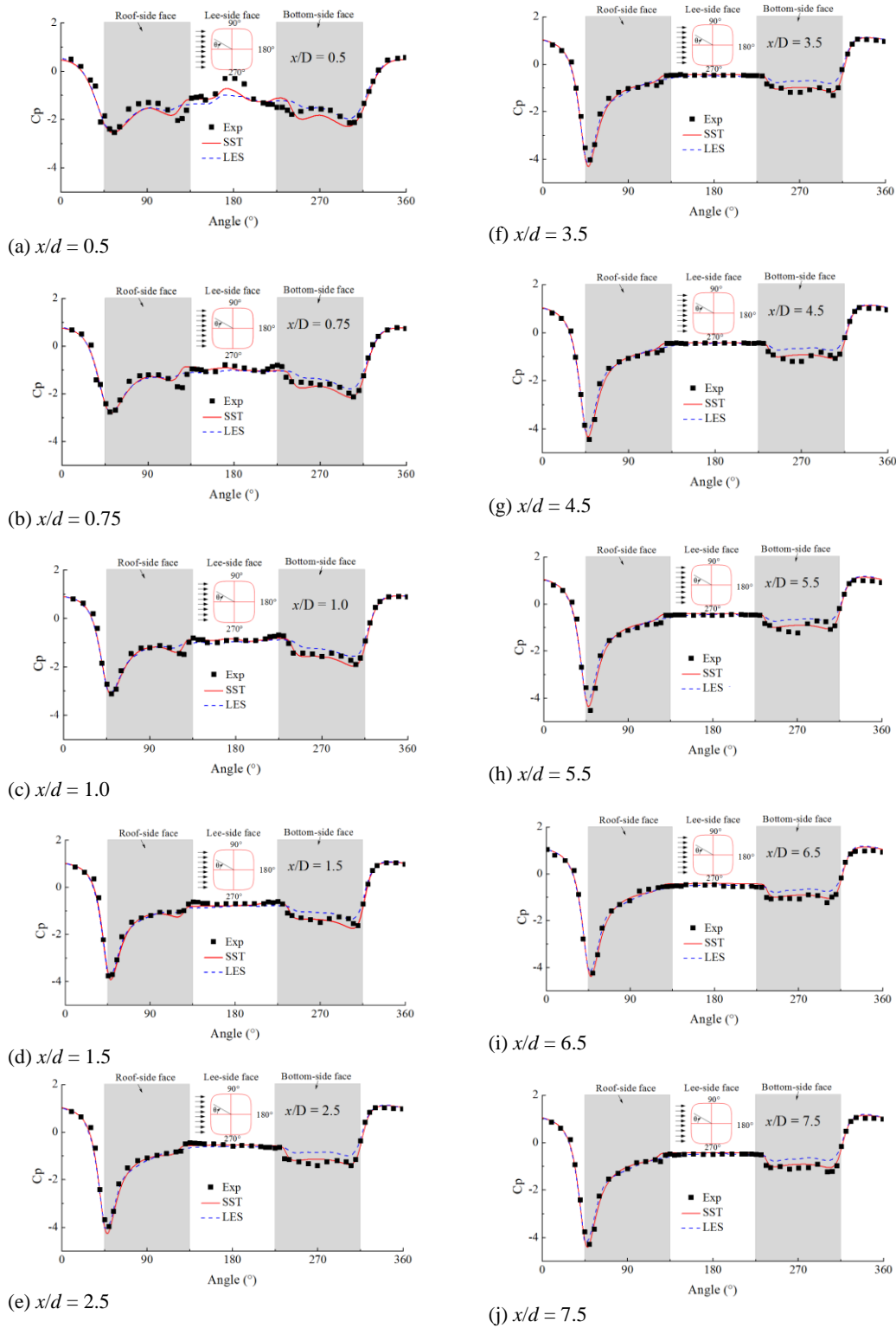


Fig. 14. Comparison of the pressure coefficient distribution on different planes.

Figure 16 shows the pressure distribution around the train and streamlines projected onto different planes. The following streamline patterns are observed:

- (1) At the train nose, two attached vortices V_1 and V_2 are appeared;
- (2) The core of vortices V_4 and V_5 are far from the lee side face;
- (3) In the region from $x/d = 3.5$ to $x/d = 7.0$, there are two stable vortices V_1 and V_3 ;
- (4) In the region with $x/d \geq 7.0$, vortex V_1

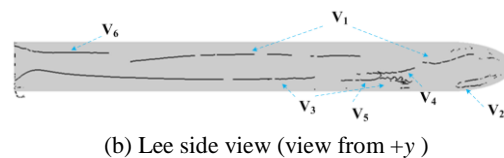
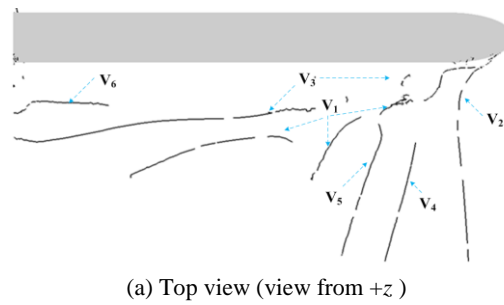


Fig. 15. Vortex cores around the train.

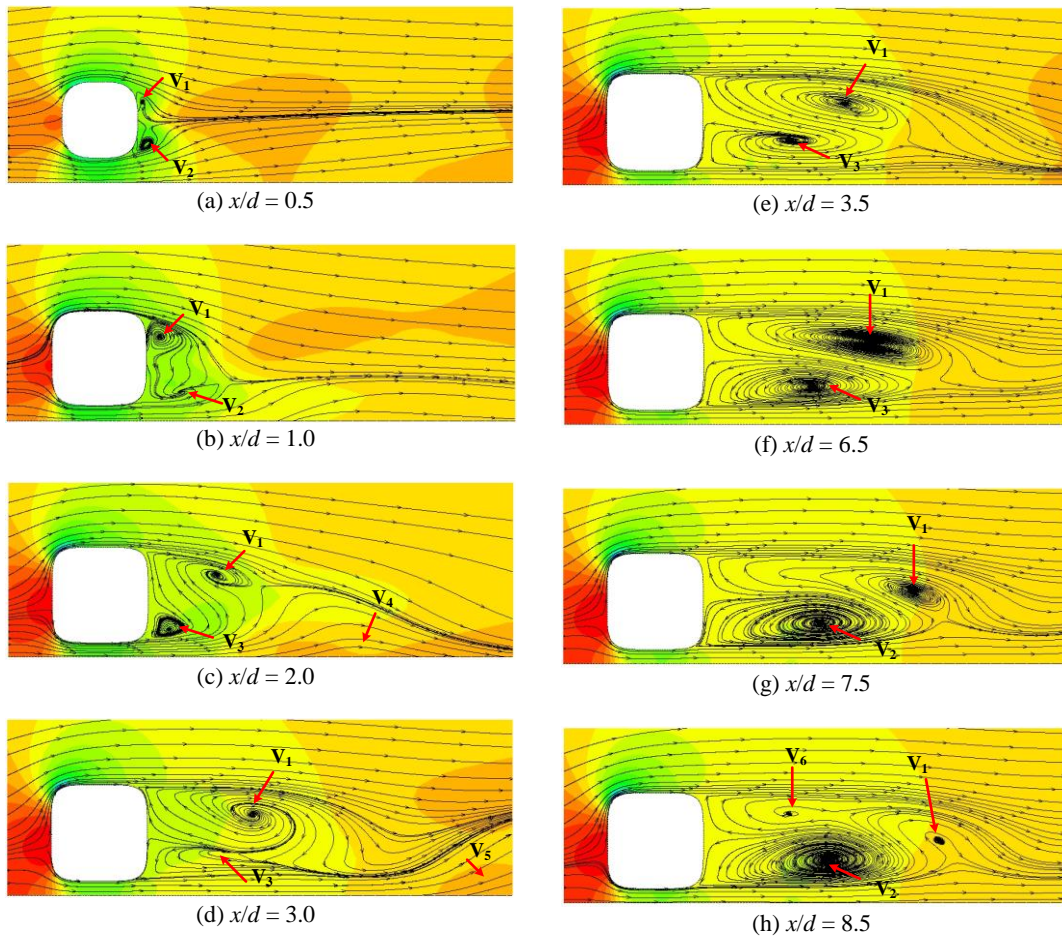
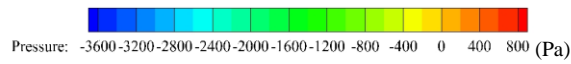


Fig. 16. Pressure distributions and streamlines around the train (colored by the pressure magnitude).

extruded by the vortex V_3 is split up into two vortices V_6 and V_1 . That's because the vortex V_3 is affected by the existence of wall near the tail. Such separation is different from the LES result (Hemida *et al.*, 2005).

Compared to the LES results (Hemida *et al.*, 2005), two small vortices in the tail part are not found in this study using the RANS models. One is occurred in the middle above the top-side face, and the other one is located at the crossing of the bottom-side and lee-side faces.

7. CONCLUSION AND DISCUSSION

The flow field around and the surface pressure on a simplified train model subjected to crosswinds were investigated using different RANS modelling validated against the experimental work conducted by Chiu *et al.* (1991). The effects of mesh size and spatial discretization schemes on the flow around the train were also investigated and the conclusions can be drawn from the results as follows:

- (1) The results showed that the second order discretization scheme is sufficient for numerical simulations of aerodynamic characteristics of trains subjected to crosswinds and discretization of higher order discretization schemes with RANS modeling is not needed. The first order scheme was unable to accurately predict the minimum pressure occurred at the crossing of the roof-side and windward-side faces, which affects both the side and lift force coefficients.
- (2) All RANS modelling overestimated the surface pressure on the bottom-side face when y^+ is around 30.0 and the standard wall function is adopted. Although the side force coefficient obtained using the standard $k-\varepsilon$ model together with the standard wall function is close to the expected one, the pressure on the lee-side face deviated from the experimental one at some cross-sections along the train length.
- (3) Among all turbulence modelling, the SST $k-\omega$ model with a low y^+ provided the accurate aerodynamic coefficients and pressure distribution, with comparison to the experimental data, and the standard $k-\omega$ model performs the second best.
- (4) The pressure distribution obtained from SST with the LES data of Hemida *et al.* (2005) and experimental results (Chiu *et al.*, 1992) were compared. Both SST and LES are able to reproduce accurate pressure results on almost all loops when compared to experimental data. Compared to the LES results, the SST $k-\omega$ model predicts more accurate results on the bottom-side face at all loops except the $x/d = 0.5$. The fine mesh used by Hemida *et al.* (2005) was, however, 11.5 million, which is less than that, used for the SST $k-\omega$ model and that could be a reason of the better performance.

ACKNOWLEDGEMENTS

This project is supported by the National Natural Science Foundation of China (No. 51605397, 51705267), Science and Technology Project of Sichuan Province (No.19YYJC0683) and the Research Project of State Key Laboratory of Traction Power (No. 2016TPL_T02).

REFERENCES

- Baker, C. J. (1986). Train aerodynamic forces and moments from moving model experiments. *Journal of Wind Engineering and Industrial Aerodynamics* 24, 227-251.
- Baker, C. J. (2010). The simulation of unsteady aerodynamic crosswind forces on trains. *Journal of Wind Engineering and Industrial Aerodynamics* 98, 88-99.
- Baker, C. J., S. J. Dalley, T. Johnson, *et al.* (2001). The slipstream and wake of a high-speed train. *Proc. IMechE Part F: J. Rail and Rapid Transit* 215, 83-99.
- Baker, C. J., J. Jones, F. Lopez-calleja, *et al.* (2004). Measurements of the cross wind forces on trains. *Journal of Wind Engineering and Industrial Aerodynamics* 92, 547-563.
- Bocciolone, M., F. Cheli, R. Corradi, *et al.* (2008). Crosswind action on rail vehicles: Wind tunnel experimental analyses. *Journal of Wind Engineering and Industrial Aerodynamics* 96, 584-610.
- BS EN. (2010), Railway applications - Aerodynamics - Part 6: Requirements and test procedures for cross wind assessment, EN 14067-6.
- Cheli, F., F. Ripamonti, D. Rocchi, *et al.* (2010). Aerodynamic behaviour investigation of the new EMUV250 train to cross wind. *Journal of Wind Engineering and Industrial Aerodynamics* 98, 189-201.
- Chiu, T. W. and L. C. Squire (1992). An Experimental Study of the Flow Over a Train in a Crosswind at Large Yaw Angles up to 90°. *Journal of Wind Engineering and Industrial Aerodynamics* 45, 47-74.
- Cooper, R. K. (1981). The effect of cross-winds on trains. *J. Fluids Eng.* 103, 170-178.
- Copley, J. M. (1987). The Three-Dimensional Flow Around Railway Trains. *J. Wind. Eng. Ind. Aerodyn.* 26, 21-52.
- Diedrichs, B. (2003). On computational fluid dynamics modeling of crosswind effects for high-speed rolling stock. *Proc. IMechE Part F: J. Rail and Rapid Transit* 217, 203-226.
- Diedrichs, B. (2010). Aerodynamic Crosswind Stability of a Regional Train Model. *Proc. IMechE Part F: J. Rail and Rapid Transit* 224, 580-591.
- Diedrichs, B., M. Sima, A. Orellano, *et al.* (2007). Crosswind stability of a high-speed train on a high embankment. *Proc. IMechE Part F: J. Rail and Rapid Transit* 221, 205-225.
- Ding, Y., M. Sterling and C. J. Baker (2008). An alternative approach to modeling train stability in high cross winds. *Proc. IMechE Part F: J. Rail and Rapid Transit* 222, 85-97.

- Dorigatti, F., M. Sterling, C. J. Baker, *et al.* (2015). Crosswind effects on the stability of a model passenger train - A comparison of static and moving experiments. *Journal of Wind Engineering and Industrial Aerodynamics* 138, 36-51.
- Flynn, D., H. Hemida, D. Soper, *et al.* (2014). Detached-eddy simulation of the slipstream of an operational freight train. *Journal of Wind Engineering and Industrial Aerodynamics* 132, 1-12.
- García, J., J. Muñoz-Paniagua, A. Jiménez, *et al.* (2015). Numerical study of the influence of synthetic turbulent inflow conditions on the aerodynamics of a train. *Journal of Fluids and Structures* 56, 134-151.
- Hemida, H. and C. Baker (2010). LES of the flow around a freight wagon subjected to crosswind. *Computers & Fluids* 39, 1944-1956.
- Hemida, H. and S. Krajnović (2008). LES study of the influence of a train nose shape on the flow structures under cross-wind conditions. *J Fluid Eng.* 130, 091101.
- Hemida, H. and S. Krajnović (2010). LES study of the influence of the nose shape and yaw angles on flow structures around trains. *Journal of Wind Engineering and Industrial Aerodynamics* 98, 34-46.
- Hemida, H., S. Krajnović and L. Davidson (2005). Large-Eddy Simulations of the Flow Around a Simplified High Speed Train Under the Influence of a Cross-Wind. *AIAA Paper No. AIAA-2005-5354*.
- Huang, S., H. Hemida and M. Z. Yang (2014). Numerical calculation of the slipstream generated by a CRH2 high-speed train. *Proc. IMechE Part F: J. Rail and Rapid Transit* 230, 1-14.
- Li, T., H. Hemida, J. Y. Zhang, *et al.* (2018). Comparisons of shear stress transport and detached eddy simulations of the flow around trains. *Journal of Fluids Engineering* 140(11), 111108.
- Li, T., M. G. Yu, J. Y. Zhang, *et al.* (2015). A fast equilibrium state approach to determine interaction between stochastic crosswinds and high-speed trains. *Journal of Wind Engineering and Industrial Aerodynamics* 143, 91-104.
- Liu, T. H., Z. W. Chen, X. S. Zhou, *et al.* (2018). A CFD analysis of the aerodynamics of a high-speed train passing through a windbreak transition under crosswind. *Engineering Applications of Computational Fluid Mechanics* 12:1, 137-151.
- Maleki, S., D. Burton and M. C. Thompson (2017). Assessment of various turbulence models (ELES, SAS, URANS and RANS) for predicting the aerodynamics of freight train container wagons. *Journal of Wind Engineering and Industrial Aerodynamics* 170, 68-80.
- Matschke, G. and C. Heine (2002). Full Scale Tests on Side Wind Effects on Trains. Evaluation of Aerodynamic Coefficients and Efficiency of Wind Breaking Devices. *TRANSAERO - a European initiative on transient aerodynamics for railway system optimisation* (Springer-Verlag, Berlin, Heidelberg, and New York). ISBN 3-540-43316-3, 27-38.
- Morden, J. A., H. Hemida and C. J. Baker (2015). Comparison of RANS and Detached Eddy Simulation results to wind-tunnel data for the surface pressures upon a Class 43 High-Speed Train. *ASME J. Fluids Eng.* 137, 041108.
- Östh, J. and S. Krajnović (2014). A study of the aerodynamics of a generic container freight wagon using large-eddy simulation. *J.Fluids Struct.* 44, 31-51.
- Premoli, A., D. Rocchi, P. Schito, *et al.* (2016). Comparison between steady and moving railway vehicles subjected to crosswind by CFD analysis. *Journal of Wind Engineering and Industrial Aerodynamics* 156, 29-40.
- Schetz, J. A. (2001). Aerodynamics of high-speed trains. *Annual Review of Fluid Mechanics* 33, 371-414.
- Suzuki, M., K. Tanemoto and T. Maeda (2003). Aerodynamic characteristics of train/vehicles under cross winds. *Journal of Wind Engineering and Industrial Aerodynamics* 91, 209-218.
- Xiong, X. H., X. F. Liang, G. J. Gao, *et al.* (2006). Train aerodynamic characteristics in strong crosswind on Lanzhou-Xinjiang railway line. *Journal of Central South University* 37(6), 1183-1188.